



Article

Complex Speciation and Distribution of Iron, Sulfur, and Trace Metals in Coal Mine Soils Reflect Grain- and Sub-Grain-Scale Heterogeneity during Pyrite Oxidative Dissolution

Md Abu Raihan Chowdhury and David M. Singer *

Department of Earth Sciences, Kent State University, Kent, OH 44242, USA; mchowdh7@kent.edu

* Correspondence: dsinger4@kent.edu

Abstract: Historical coal mining practices have caused various soil and water hazards, particularly through the dumping of mine waste. The primary environmental risk associated with this waste is the leaching of toxic metals from dumps of spoil or refuse into the subsurface soil or into nearby water resources. The extent of metal release is controlled via the oxidative dissolution of pyrite and potential re-sequestration through secondary Fe oxides. The characterization of the dominant Fe-bearing phase and the distribution of trace metals associated with these phases was determined via electron microscopy, synchrotron-based X-ray micro-fluorescence (μ -XRF) element and redox mapping from shallow mine soils from an impacted watershed in Appalachian Ohio. The dominant Fe-bearing phases were: (1) unweathered to partially weathered pyrite; (2) pseudomorphic replacement of pyrite with Fe(III) oxides; (3) fine-grained Fe oxide surface coatings; and (4) discrete Fe(III) oxide grains. Thicker secondary coatings and larger particles were sulfate rich, whereas smaller grains and thinner coatings were sulfate poor. The discrete Fe oxide grains exhibited the highest concentrations of Cr, Mn, Ni, and Cu, and sub-grain-scale concentration trends (Mn > Cr > Ni > Cu) were consistent with bulk soil properties. Predicting future metal transport requires an understanding of metal speciation and distribution from the sub-grain scale to the pedon scale.



Citation: Chowdhury, M.A.R.; Singer, D.M. Complex Speciation and Distribution of Iron, Sulfur, and Trace Metals in Coal Mine Soils Reflect Grain- and Sub-Grain-Scale Heterogeneity during Pyrite Oxidative Dissolution. *Soil Syst.* **2024**, *8*, 2. <https://doi.org/10.3390/soilsystems8010002>

Academic Editor: Manfred Sager

Received: 4 October 2023

Revised: 18 December 2023

Accepted: 20 December 2023

Published: 22 December 2023



Copyright: © 2023 by the authors. Licensee MDPI, Basel, Switzerland. This article is an open access article distributed under the terms and conditions of the Creative Commons Attribution (CC BY) license (<https://creativecommons.org/licenses/by/4.0/>).

Keywords: coal mine soil; Fe oxides; trace metal sequestration; synchrotron-based redox mapping

1. Introduction

Historical coal mining practices have caused various soil, water, and air hazards to the environment and humans [1–3]. Coal mining drastically and negatively affects surface environments, particularly through the dumping of mine waste (i.e., mine spoil) [4]. It has been estimated that in Ohio alone, there are approximately 36 billion tons of known coal mine spoil spread over 600 km² [5]. Further, depending on local geology and surface mining practices, approximately a half ton of waste is produced for every ton of mined coal [6]. Further, it has been estimated that there are 32,000 km² of land in the U.S. that have been impacted by coal mining, and only 685 km² of those mines (~2%) have been reclaimed [7,8]. One of the primary environmental risks associated with this waste is the leaching of toxic metal(loid)s from dumps of spoil or refuse into the subsurface soil or into nearby water resources [1]. These elements (e.g., Cr, Mn, Cu, and Ni) are typically bound primarily within pyrite (FeS₂) and other sulfides that form during coal deposition and later diagenetic processes [9]. As the unreclaimed mine spoil weathers, the oxidative dissolution of pyrite present in the waste and mine soils can leach acidity and toxic elements, resulting in local water quality impairment [10]. Chromium and Ni are toxic and produce mutagenic, carcinogenic, and genotoxic effects; Cu can cause significant toxicological effects, and there is growing concern regarding the impact of Mn on human health and ecosystems [11,12]. It is therefore critical to fully assess the potential for metal transport from these systems.

The extent of toxic element leaching from coal mine waste is controlled using a complex set of hydrogeochemical conditions following the oxidative dissolution of pyrite.

At low pH and high concentrations of Fe and trace metals (Mn, Cu, and Ni) released from pyrite, dissolution can occur in the aqueous phase and be transported with pore water downgradient [13]. As the released acidity is consumed through further weathering reactions and pore water pH is buffered, the deposition of secondary Fe(III)-bearing phases is thermodynamically favored [14,15]. These phases can include a wide range of Fe(III)-(oxy)hydroxides and (oxy)hydroxysulfates, referred to hereafter as “Fe-oxides”. The common phases include jarosite ($\text{KFe}_3(\text{SO}_4)_2(\text{OH})_6$), schwertmannite ($\text{Fe}_8\text{O}_8(\text{OH})_{8-2x}(\text{SO}_4)_x$ with $1 \leq x \leq 1.75$), ferrihydrite (approximately $5\text{Fe}_2\text{O}_3 \cdot 9\text{H}_2\text{O}$), goethite (FeOOH), and hematite (Fe_2O_3), with varying texture and morphology based on the combined effects of pore water composition, rainwater infiltration, and mine soil porosity and permeability [16–18]. Further, local micro-zones may also control the formation and transition between phases through the changes in pH, Eh, and pore connectivity [19–21].

In this study, we examined the dominant Fe-bearing phases that formed following oxidative pyrite dissolution in soils developing on historic mine spoils to explore the range of weathering outcomes. The formation and transformations of secondary Fe oxides can impact pore water composition by re-sequestering trace metals released from pyrite weathering [22–24]; however, the efficacy of secondary uptake is controlled by Fe oxide composition, grain size and texture, and local pore water conditions. It was hypothesized that fine-grained secondary Fe oxides with a high surface would dominate metal re-sequestration. This work also aimed to gauge the potential future release of toxic elements, as predicting future metal transport requires an understanding of metal speciation and distribution from the sub-grain scale to the pedon scale. In the current study, electron microscopy and synchrotron-based X-ray micro-fluorescence (μ -XRF) element and redox mapping were used to determine: (1) the texture, morphology, and composition of the dominant Fe-bearing phase in these soils; and (2) the distribution of trace metals associated with these phases. Trends in metal enrichment in secondary Fe oxides were also compared to trends in bulk metal concentrations in the parent coal shale and the mine soils.

2. Materials and Methods

2.1. Site Description

The study site HR-25, sub-watershed #25 of Huff Run watershed, contains an abandoned underground mine area located near Mineral City, Ohio (Figure 1). This area experienced extensive coal mining operations from 1890 to 1946 [25]. After 1946, the site was abandoned, leaving all mine spoils and underground mine tunnels unreclaimed. The oxidation of pyrite present in the coal and sedimentary formation led to a massive acid mine drainage (AMD) generation, which severely impacted the surface and groundwater condition in HR-25 [25]. To date, remediation projects installed at the site since 1996 have cost USD 590,000, which has curbed the AMD release from the site and significantly improved the surface water. However, despite the success in improving the surface water quality, abandoned mine waste and spoils continue to leach non-point sources (e.g., mine spoils) and have the potential to continually release toxic elements over a time period of approximately decades, resulting in ongoing negative impacts on the local ecosystem. Previous studies have focused on abandoned spoils adjacent to the current study sites [26–29], and these previous projects provide further information about the history, climate, and remediation activities of the Huff Run Watershed and sub-watershed 25.

2.2. Soil Sample Collection, Thin-Section Preparation, and Grain-Scale Characterization

Shallow soil samples (0–10 cm) were collected in 2016 from two locations within HR-25; these soils have been extensively studied to determine the relationship between bulk mineralogy, geochemistry, and pore water composition [29], the relationship between trace metal transport and the presence of secondary mineral surface coatings [26], and the importance of colloid transport of trace metals [29,30]. Site 1 is located at the bottom of a mine spoil heap adjacent to a tributary (known as the HR-25 tributary); site 2 is located at the bottom of another mine spoil heap further uphill of site 1 (Figure 1). Site 1 has a shallow

slope with sparse grass and a few trees, whereas site 2 has a steeper slope and minimal vegetation. Site 1 had a thin (<2 cm) organic layer, while site 2 did not exhibit an organic layer. These mine soils have been reported to exhibit a loam-type texture [27] with pore water pH values of approximately 5.5 [28].

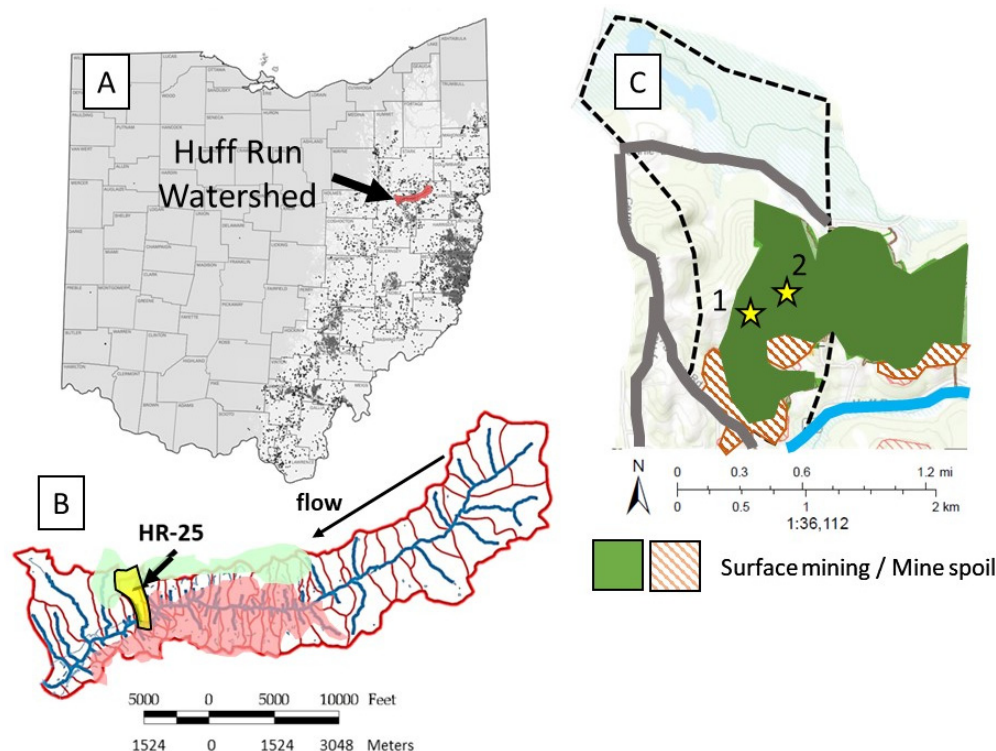


Figure 1. (A) Location of the Huff Run Watershed (in red), with Ohio coal counties shown in light gray and known abandoned coal mines in dark gray [31]; (B) a watershed map [32] showing the location of sub-watershed HR-25 (in yellow), stream flow direction, and portions of the watershed impacted by historic surface mines and abandoned mine spoils (pink) and areas that still have active permits (green); (C) Map of sub-watershed HR-25 (the dashed outline), which includes the spatial extent of known surface area affected by coal surface mining (green) and mine spoil emplacement (hatched orange), the Huff Run stream (blue line) and roads (gray lines). The stars represent sampling sites 1 and 2. The coal mining data were obtained from: <https://gis.ohiodnr.gov> (accessed on 7 December 2014).

2.3. Characterization of Fe, S, and Trace Metal Speciation and Distribution

A subset of these soils was air-dried and passed through a 1-mm sieve following field sampling, embedded in epoxy (EPO-TEK 301-2FL) and polished using kerosene instead of water to prevent redox changes from occurring during thin-section preparation. The samples were cut to ~30 μm thick and mounted onto high-purity quartz glass slides (Spectrum Petrographics, Inc., Vancouver, WA, USA). The grain size, texture, morphology, and composition of soil minerals were determined using a Hitachi Benchtop TM3030 scanning electron microscope (SEM) equipped with energy-dispersive spectroscopy (EDS; Quantax70), operated at 15 keV voltage, with a spot size of 10 nm, and a detector-to-sample working distance typically of 10 mm. Micro-XRF analyses were performed at beamline 13-ID-E at the Advanced Photon Source [33]. The synchrotron beam size for $\mu\text{-XRF}$ was 2 $\mu\text{m} \times 2 \mu\text{m}$, focused using a Pt-coated Kirkpatrick–Baez (K–B) focusing optical system (XRadia, Zeiss Microscopy, Pleasanton, CA, USA). A four-element Si vortex detector (SSD, Hitachi, Tokyo, Japan) was used for X-ray fluorescence data collection. Monochromatic X-rays were selected using a water-cooled Si(111) ($\phi = 90$) double-crystal monochromator. Multiple maps were collected near the S–K edge ($E_0 = 2474 \text{ eV}$) (for S) and the Fe–K edge

($E_0 = 7112$ eV) (for Fe) and at 13 keV for other elements (Si, P, S, K, Ca, Ti, V, Cr, Mn, Fe, Ni, Cu, and Zn). Data were collected at a 2 μm pixel size and 50 ms dwell time per point, and fluorescent maps were analyzed using the Larch v.0.9.55 software package [34]. The measured intensity of the incident energy of the X-ray beam (I_0) was used to normalize the fluorescent counts of each energy map across each line, and the change in I_0 was less than 1%. Sulfur oxidation state speciation maps were constructed based on maps that were collected across the S–K edge (2471 eV, 2473 eV, 2478 eV, 2482 eV, and 2490 eV) to produce maps of the distribution of the operationally defined oxidation states, reduced (“ S_{red} ”, which ranges from S(-II) to S(0)) and oxidized (“ S_{ox} ”, which ranges from S(0) to S(VI)); Fe oxidation state speciation maps were constructed based on maps that were collected across the Fe–K edge (7123 eV, 7127 eV, and 7136 eV) to produce maps of Fe(II) and Fe(III) [5,24,35]. Based on the experimental setup, the distributions of Cr, Mn, Cu, and Ni were determined with maximum I_0 -normalized values of each element in the maps collected at 7136 eV of 7×10^{-4} , 3.7×10^{-3} , 9×10^{-4} , and 2×10^{-4} , respectively. Using these values as proxies for concentration results in relative concentration values (Mn > Cr > Ni > Cu) that are consistent with trace element compositions determined via the bulk XRF of soils collected from the same site [25], justifying the use of intensity counts as a proxy for concentration at the grain scale. Box-and-whisker plots were therefore created by separating regions of each map based on the dominant type of Fe-bearing phase, described below, to determine their relative trace metal content as a function of Fe speciation. For each type of Fe-bearing phase, four separate regions from each map of a representative grain or aggregate of grains were used to extract I_0 -normalized counts, which were then compiled for the box-and-whisker plots. The Fe-bearing phases of concern (pyrite and Fe oxides) were in either extremely low abundance or not detectable in the other lithologies that comprise the mine spoil. The other Fe-bearing phases (e.g., clays and organic matter) were in low abundance and were not the focus of this study.

3. Results

Based on the SEM–EDS and μ -XRF analyses, four categories of the dominant Fe-bearing phases were described based on their composition, morphology, and Fe and S redox state distributions: (1) unweathered to partially weathered pyrite; (2) pseudomorphic replacement of pyrite with Fe(III)-bearing phases, which were typically hollow; (3) fine-grained Fe(III) oxide surface coatings often co-localized in aggregates with clays, covering primary silicate grains; and (4) discrete Fe(III) oxide grains. Other Fe-bearing phases, such as clays and organic matter, were observed as minor constituents and were not the focus of this work. The distribution of Fe and S redox states and the association of trace metals with each of the four types of Fe-bearing phases are discussed below. The four types of Fe phases were observed in samples from sites 1 and 2, and the text below does not differentiate the results between the two sites; representative SEM–EDS and μ -XRF analyses from both sites are highlighted in the figures.

3.1. Unweathered to Partially Weathered Pyrite

The SEM–EDS analyses of the soil samples showed the presence of grains with their morphologies and compositions consistent with unweathered to partially weathered pyrite in the soils forming on mine spoils (Figure 2). These Fe–S-rich phases were commonly present in relatively larger aggregates of Fe–O-rich grains (likely secondary Fe oxides) and/or clay minerals (Figure 2). The pyritic Fe–S-rich grains themselves were typically 2–10 μm (Figure 2A,C), and pyritic grains greater than ~ 10 μm were less commonly observed. The Fe–O-rich aggregates were usually larger in size (~ 200 μm , Figure 2A) compared to the clay-rich aggregates (35–40 μm at their widest dimension, Figure 2C). The relatively smaller frambooids of pyrite were present in a loosely packed aggregate and showed physical signs of oxidative weathering, resulting in an uneven frambooidal/euhedral morphology (Figure 2B). Pyritic grains that were smaller and/or embedded in thinner aggregates exhibited depleted Fe and S concentrations, based on the EDS analyses, compared to

larger, unweathered pyritic grains in thicker aggregates. The larger grains also tended to exhibit euhedral shapes with sharp contact boundaries (Figure 2C).

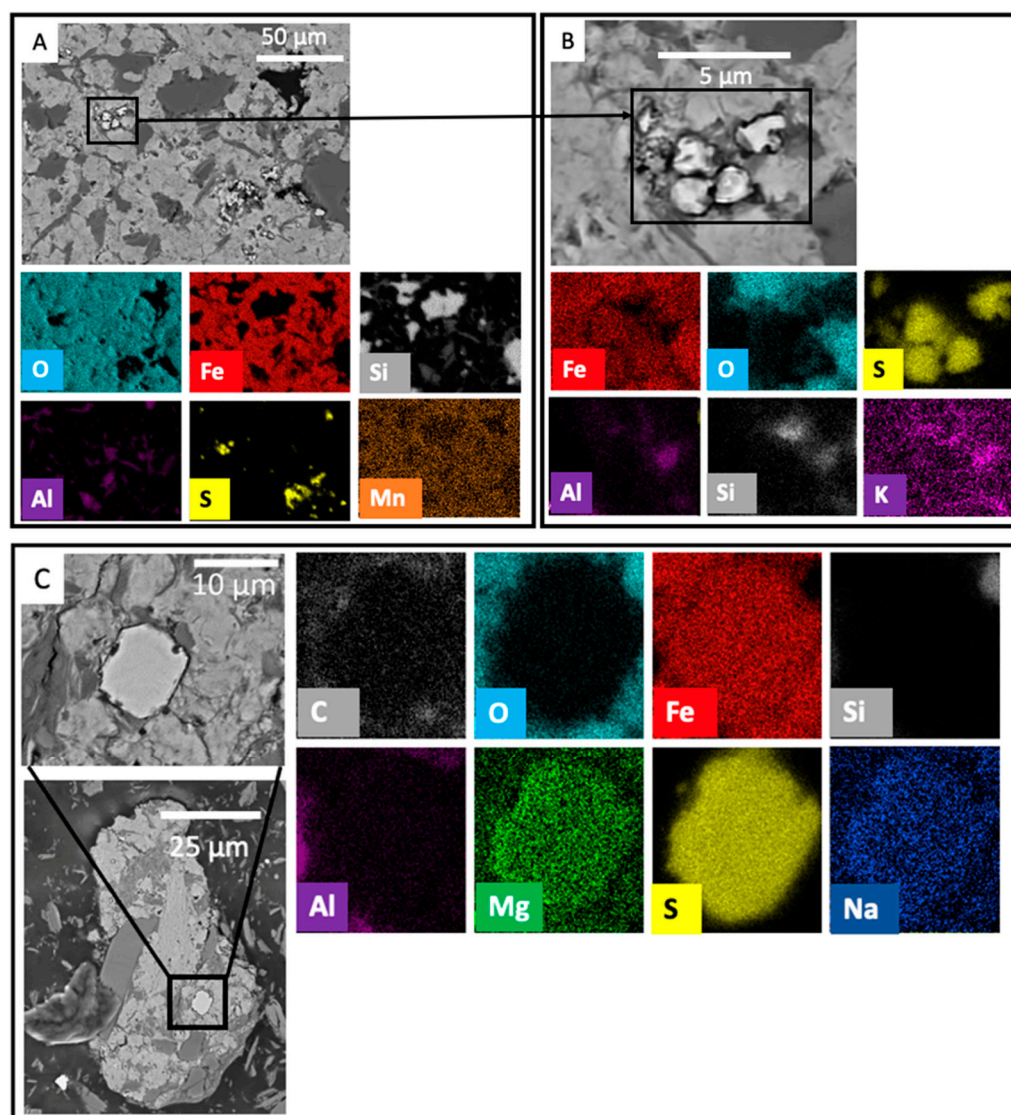


Figure 2. Representative SEM backscattered electron images and EDS elemental maps of grains consistent with the composition and morphology of framboidal pyrite, showing evidence of dissolution pits and weathering features for sites 1 (A,B) and 2 (C). The black box in (A) indicates the field of view in (B); the black box in (B) indicates the EDS map regions. The black box in (C) indicates the EDS map region of a grain with its morphology and composition consistent with a euhedral grain of pyrite that is protected from dissolution from a complex matrix of grains dominated by grains consistent with phyllosilicate composition and textures.

The presence of unweathered and partially weathered pyritic grains was confirmed by the μ -XRF analyses, which indicated the presence of Fe(II)- S_{red} -dominated grains that were approximately 5 μ m in diameter (Figure 3). The presence of partially weathered pyrite grains was not observed in the μ -XRF analyses, likely because the spatial distribution of the chemical features associated with these grains is lower than the spatial resolution of the μ -XRF analyses. However, grains characteristic of weathering products that were Fe(III) rich and S poor were typically aggregated around the pyritic grains and were approximately 10–20 μ m in diameter (Figure 3, left column). A number of pyritic grains lacked surface coatings at the resolution of the μ -XRF analyses (Figure 3, right column) and

were not present in the aggregates with Fe oxides or clays; however, it is possible that these grains were liberated from soil aggregates during sample collection and preparation. The concentrations of Cr, Mn, Ni, and Cu, based on I0-normalized μ -XRF counts, associated with pyritic grains were typically low (Figure 3) and were the lowest of the four types of Fe-bearing phases in the soils based (Figure 4). However, the concentrations of these metals in all four types of Fe-bearing phases, including pyrite, were higher compared to the total sample concentration (Figure 4).

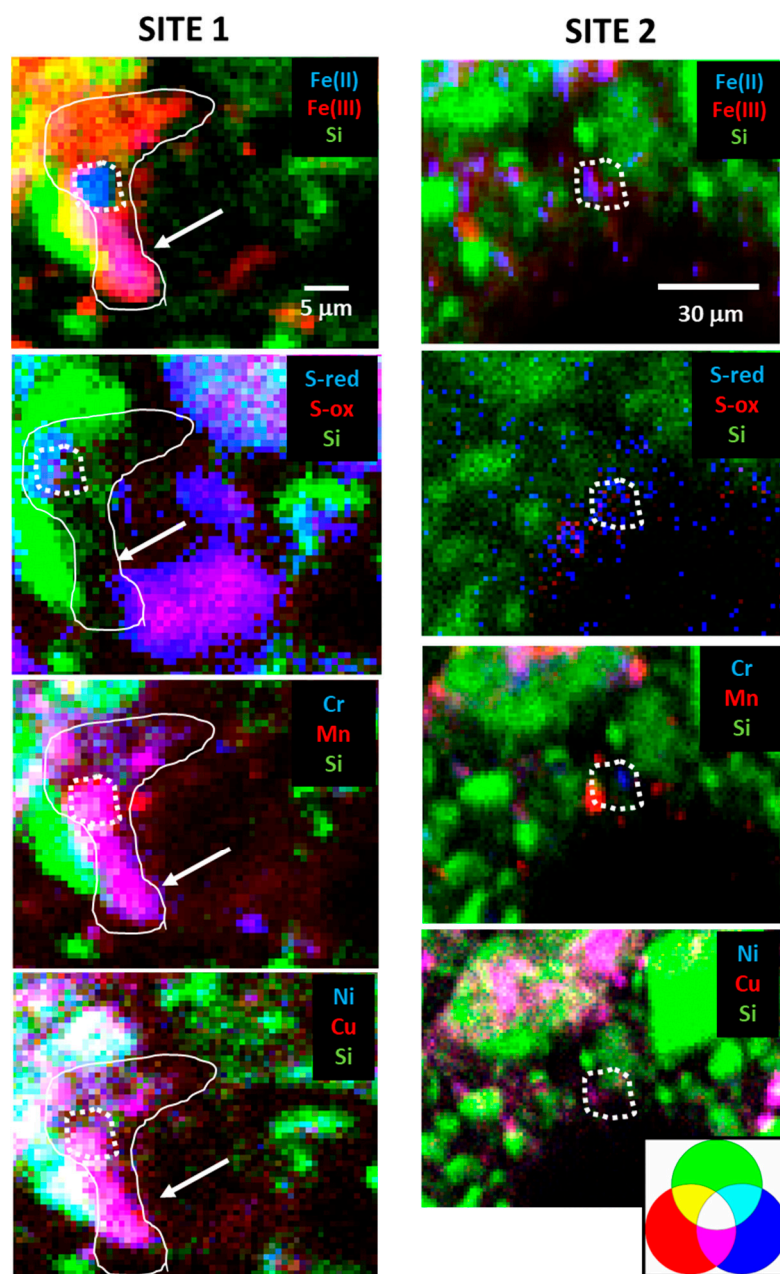


Figure 3. Representative μ -XRF images for unweathered pyrite (regions in white-dashed lines) and weathered products (regions in a solid white line and highlighted by the white arrow), including redox maps (for Fe and S) and elemental maps (for Si, Cr, Mn, Ni, and Cu) for the samples from site 1 (left column) and site 2 (right column). The Fe and S maps are shown as two-component images (Fe(II) and Fe(III); S_{red} and S_{ox}) plus Si for orientation relative to the other maps. The color key is shown at the bottom right.

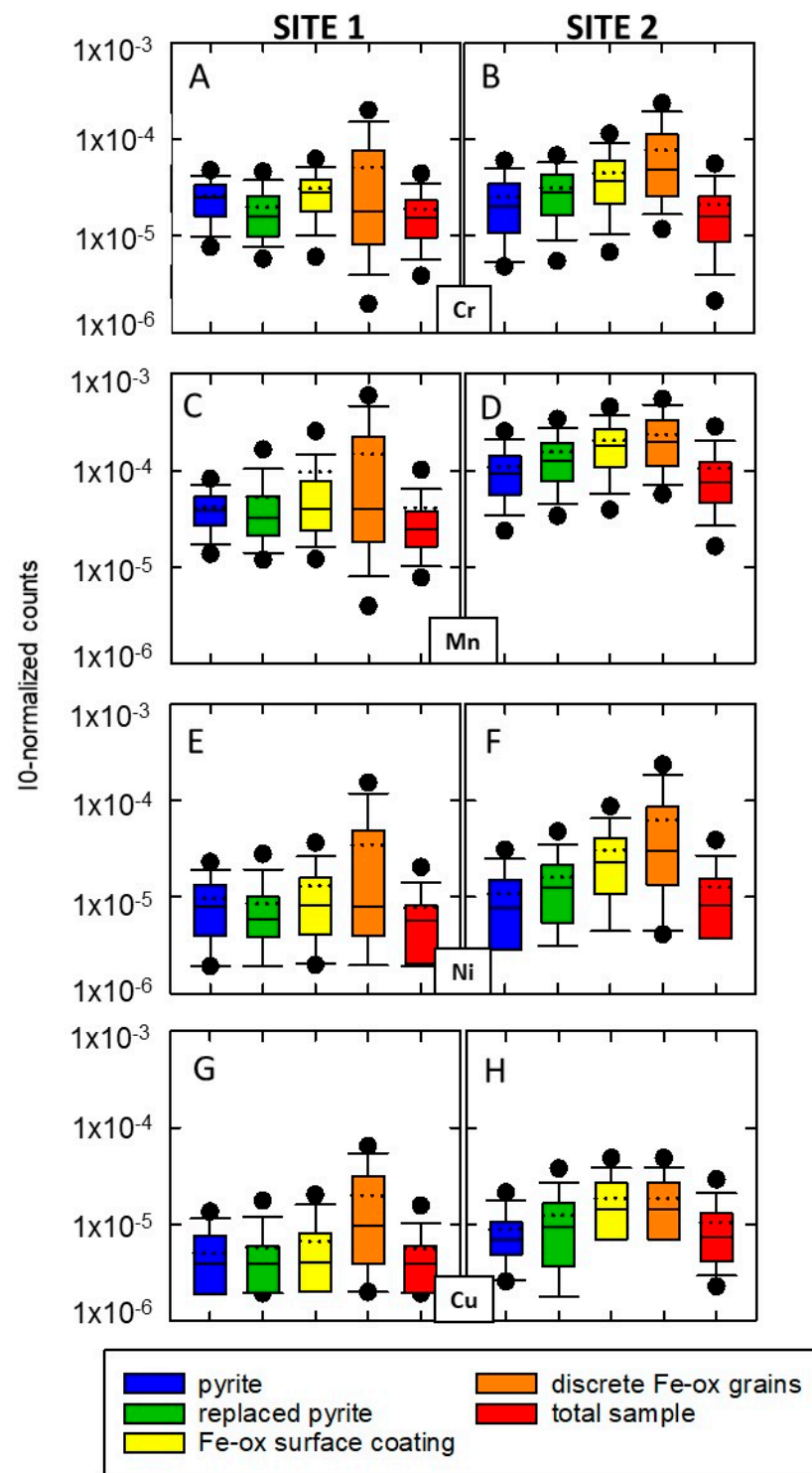


Figure 4. Box-and-whisker plots showing I₀-normalized m-XRF counts as a proxy for the concentrations of Cr (A,B), Mn (C,D), Ni (E,F), and Cu (G,H) in the samples from sites 1 (left) and 2 (right) as a function of the type of Fe-bearing host phases: pyrite (blue), pseudomorphic replacement of pyrite with Fe oxides (green), Fe oxide surface coatings (yellow), and larger discrete grains of Fe oxides (orange). The range of total metal counts for the m-XRF maps is shown in red. Median values are shown as black-dashed lines, and the black circles represent the 5th and 95th percentile of outliers.

3.2. Partial to Complete Pseudomorphic Replacement of Pyrite

Thin, hexagonal to semi-circular Fe–O-rich rinds were observed in cross-sections around cavities that are consistent with the formation of partial to complete pseudomorphic replacement of primary framboidal pyrite with Fe oxides. The Fe–O-rich layer varies from less than 1 μm (Figure 5A) to approximately 20 μm (Figure 5B). The pre-existing pyrite grains varied from approximately 1 μm (Figure 5A) to 100 μm (Figure 5B). Unweathered pyrite framboids were often observed within aggregates with fully weathered and pseudomorphically replaced pyrite framboids (replaced with Fe oxide, Figure 5B). In several cases, Fe–S-rich cores were observed covered in S-depleted rims (Figure 5B).

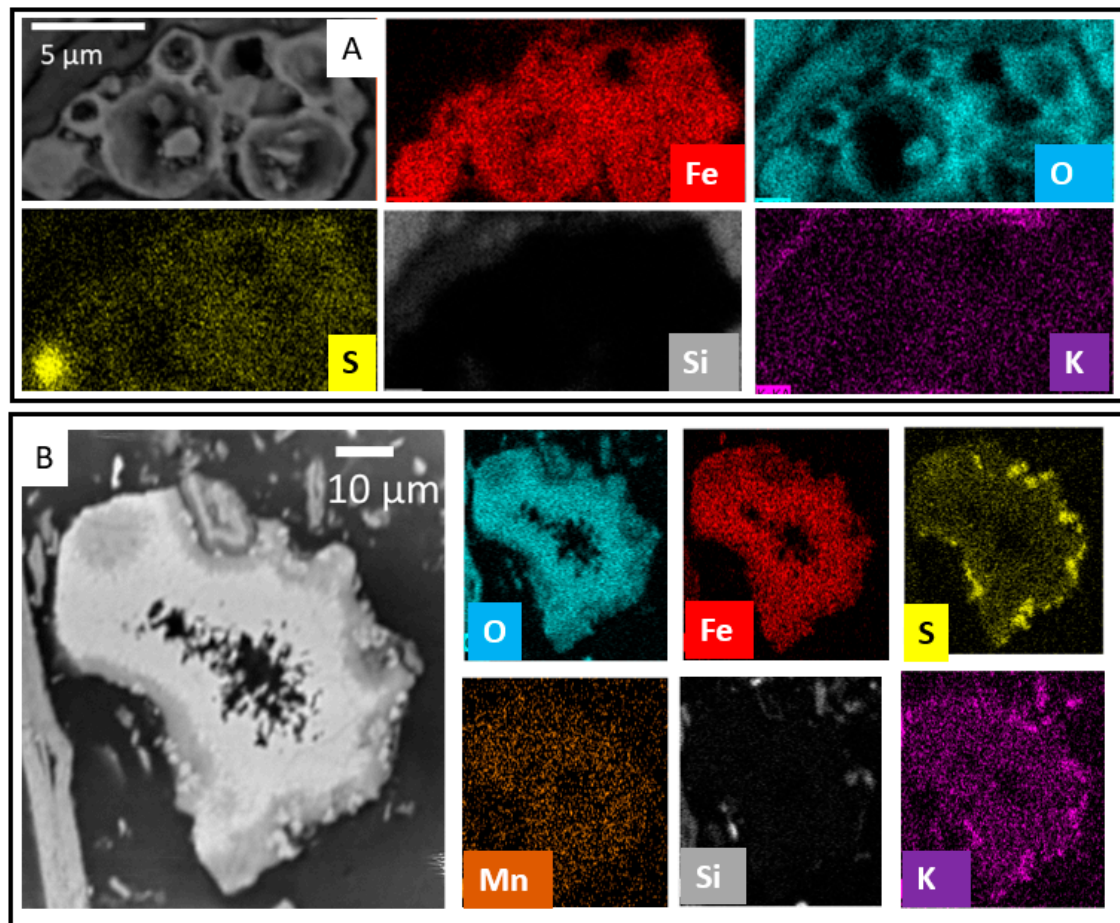


Figure 5. Representative SEM backscattered electron images and EDS elemental maps of Fe oxide pseudomorphically replacing framboidal pyrite with one possible unweathered pyrite remaining (in the top panel, lower left corner) and around the particle rims in the lower panel for site 1 (A) and site 2 (B).

The pseudomorphic replacement features observed via the SEM–EDS analyses were not detected via the μ -XRF analyses and were likely below the detection limit of the μ -XRF spatial resolution. However, pyritic cores (dominated by Fe(II) and S_{red}) with oxidized rims (dominated by Fe(III) with little S) were observed (Figure 6). The trace metal loading of the pseudomorphically replaced pyrite was typically low and dominated by Mn (Figures 5 and 6) and were higher in thicker replacement features (from ~10 to 15 μm) compared to thinner ones (<1 μm) (Figure 3). In general, the concentrations of Cr, Mn, Ni, and Cu were higher in the replacement features compared to unweathered pyrite but lower than in Fe oxide surface coatings or discrete Fe oxide grains (Figure 4).

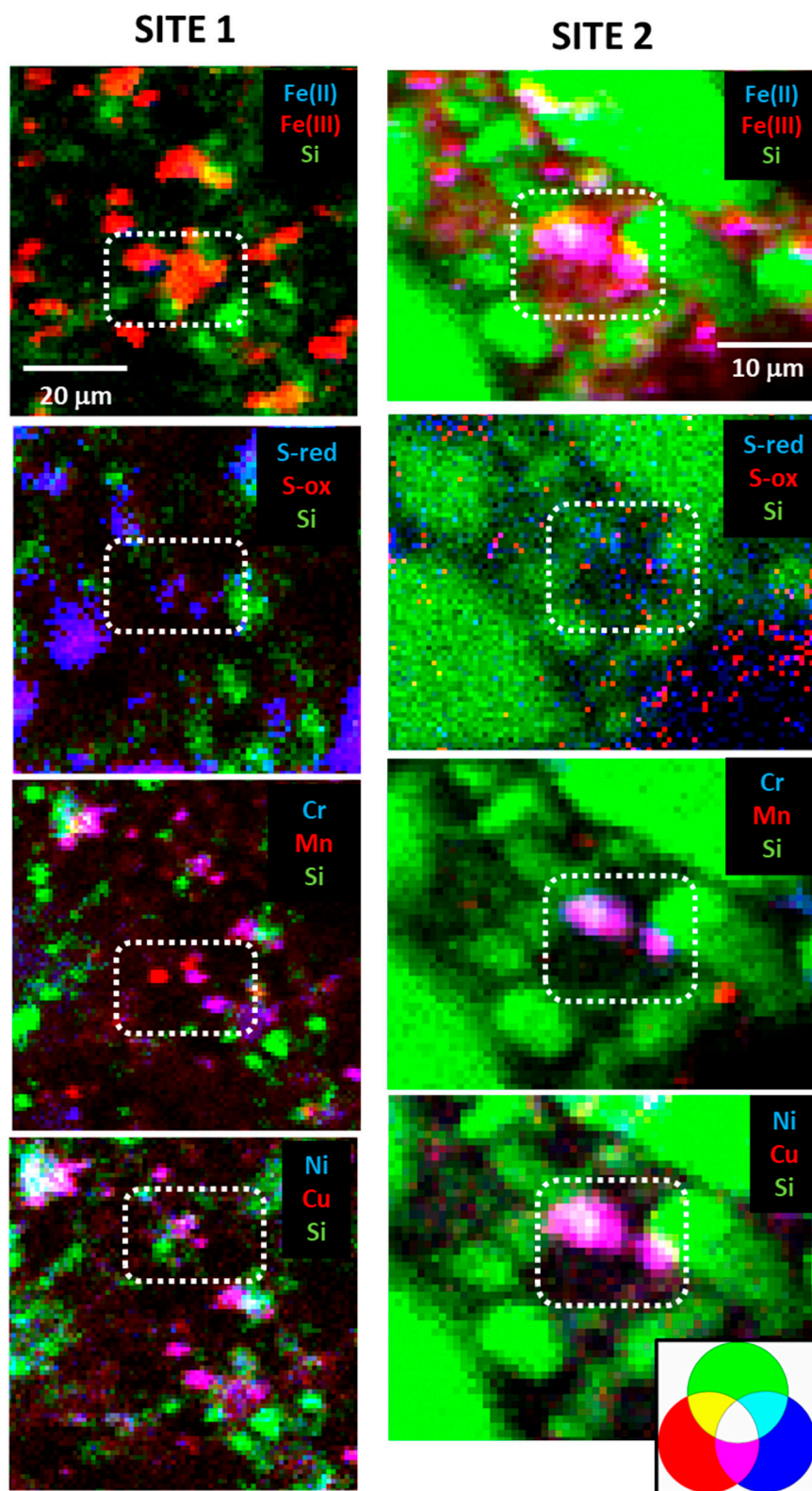


Figure 6. Representative μ -XRF images for pyrite replaced with Fe oxides (regions in white-dashed lines); structures observed in the SEM-EDS analyses were not able to be observed at the resolution of the μ -XRF analyses; however, pyritic cores with oxidized rims were observed. The images include redox maps (for Fe and S) and elemental maps (for Si, Cr, Mn, Ni, and Cu) for the samples from site 1 (left column) and site 2 (right column). The Fe and S maps are shown as two-component images (Fe(II) and Fe(III); S_{red} and S_{ox}) plus Si for orientation relative to the other maps. The color key is shown at the bottom right.

3.3. Fe Oxide Secondary Mineral Surface Coatings

Fine-grained aggregates of Fe oxides were observed as secondary mineral surface coatings (MSCs) on larger Si–O-rich grains that were likely quartz (Figure 7). The composition of the Fe MSCs were both Fe–O-rich (Figure 7A) and Fe–O–S-rich (Figure 7B), the latter of which was likely composed of Fe(III)-(oxy)hydroxides-sulfates. The MSCs typically contained aggregates of Fe-rich grains with Si–Al–O-rich grains, likely clay minerals. The MSCs were heterogeneous with respect to their thickness and coverage of the underlying grain and ranged in thickness from less than 5 μm (Figure 7A) to thicker, more physically complex aggregates that were up to 15–20 μm in thickness (Figure 7B). The thinner MSCs also tended to be dominantly Fe–O-rich, whereas the thicker ones were Fe–O–S-rich.

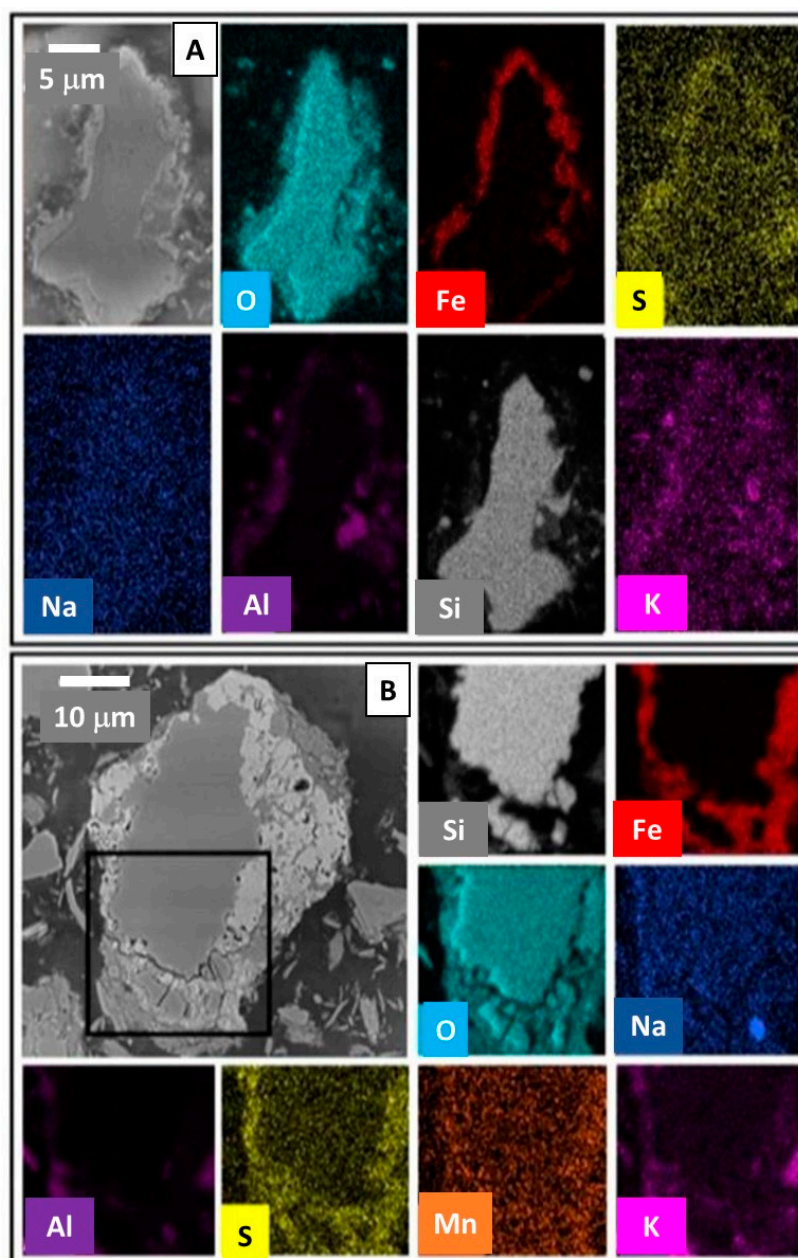


Figure 7. Representative SEM backscattered electron images and EDS elemental maps of S-bearing Fe oxide surface coatings on quartz (top panel (A), site 1), and a mix of Fe oxide and clay minerals on quartz (bottom panel (B), site 2). The black box in (B) indicates where EDS element maps were collected.

The μ -XRF analyses yielded similar results to the SEM-EDS analyses; thinner coatings were dominated by Fe(III) and were S poor, and thicker coatings were dominated by Fe(II) and Sox (Figure 8). The trace metal content in the Fe(III)-O-dominated surface coatings was the next highest of the four Fe-bearing phases in soils from sites 1 and 2 for Cr (Figure 4A,B), Mn (Figure 4C,D), and Ni (Figure 4E,F). The concentration of Cu was only higher compared to the other two Fe-bearing phases in the soil from site 2 (Figure 4H). At the grain scale, metal content was correlated with coating thickness, where thicker coatings (10–25 μ m) contained higher concentrations of Cr, Mn, Ni, and Cu, whereas thinner coatings (less than 2 μ m) exhibited a more limited trace metal content (Figure 8).

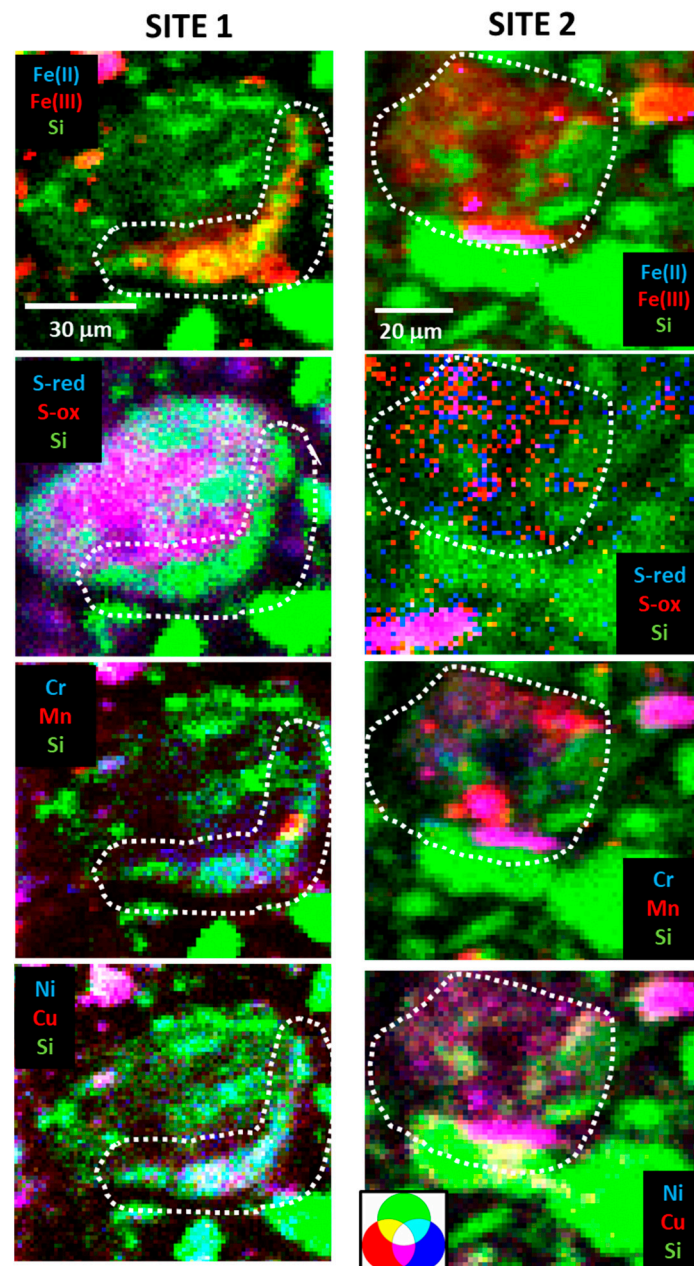


Figure 8. Representative μ -XRF images for Fe oxide surface coatings (regions in white-dashed lines), including redox maps (for Fe and S) and elemental maps (for Si, Cr, Mn, Ni, and Cu) for the samples from site 1 (left column) and site 2 (right column). The Fe and S maps are shown as two-component images (Fe(II) and Fe(III); S_{red} and S_{ox}) plus Si for orientation relative to the other maps. The color key is shown at the bottom right.

3.4. Discrete Secondary Fe-Bearing Phases

Discrete Fe-bearing grains, ranging in size from 10 μm to 20 μm to over 200 μm , were observed that were typically irregularly shaped with compositions dominated by Fe–O–S and were likely Fe(III)-(oxy)hydroxides-sulfates. Some of these discrete grains contained Si-rich inclusions (Figure 9A) and were likely clay grains incorporated during precipitation, whereas other discrete grains appeared to be relatively homogeneous single crystals (Figure 9B,C). The inclusion-bearing grains tended to have slightly lower S concentrations compared to the inclusion-free grains. Some of the larger discrete Fe grains were covered in fine-grained Si–O–Al–K-rich phases that are likely clay minerals and were up to 20 μm in thickness (Figure 9C).

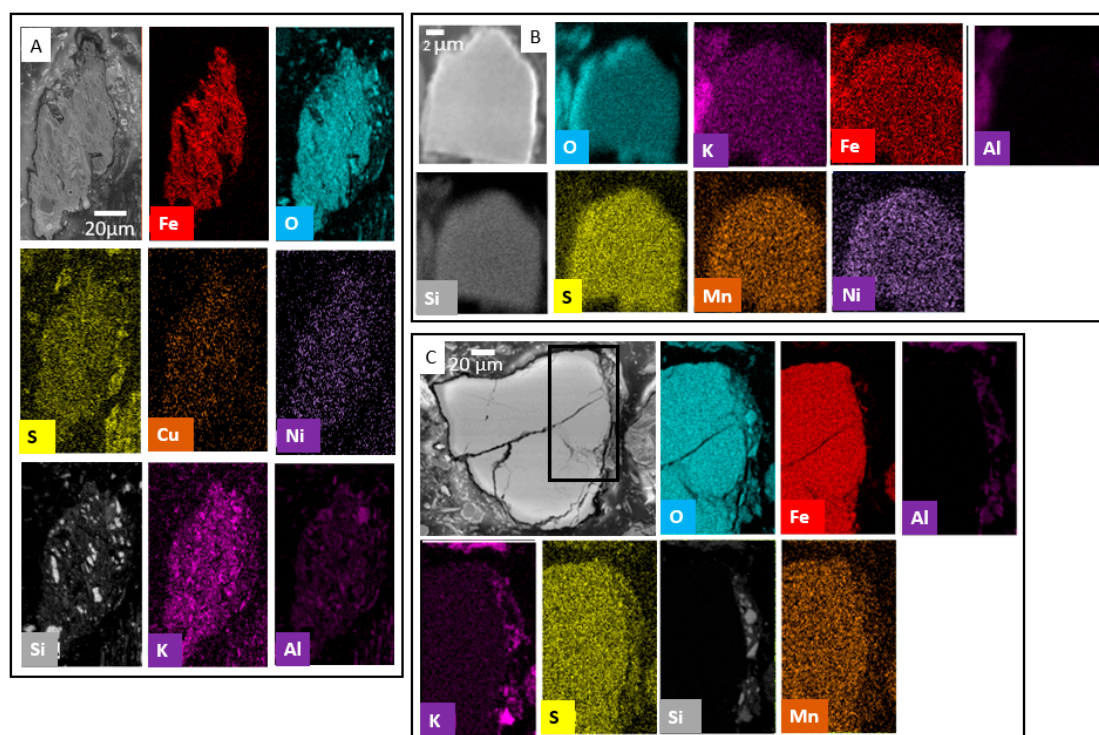


Figure 9. Representative SEM backscattered electron images and EDS elemental maps of a grain consistent with an Fe sulfate grain in an aggregate with clay particles ((A), site 1), and discrete particles of Fe sulfate ((B,C), site 2). The black box in (C) indicates where EDS element maps were collected.

The μ -XRF analyses were deemed to be consistent with the SEM–EDS analyses; smaller Fe-rich discrete grains (less than 5 μm) were Fe(III) rich and S poor, whereas larger grains were rich in both Fe(III) and S_{ox} (Figure 10). The larger grains were observed in the aggregates with Si-rich grains, although no Si-rich surface coatings were observed. However, the coatings observed via SEM–EDS were likely below the spatial detection limit of the μ -XRF analyses. Among the four Fe-bearing phases, the discrete Fe oxide grains exhibited significantly higher concentrations of Cr, Mn, Ni, and Cu compared to the other Fe-bearing phases in soils from both sites 1 and 2 (Figure 4), consistent with the SEM–EDS analyses. At the grain scale, trace metal content was correlated with the composition of the larger Fe-bearing grains, where Cu was associated with Fe(III)–O-rich phases (Figure 10), whereas Ni was associated with Fe(III)–O– S_{ox} -rich grains (Figure 6), and Mn and Cr were observed in pool types of large Fe(III) phases (Figure 10).

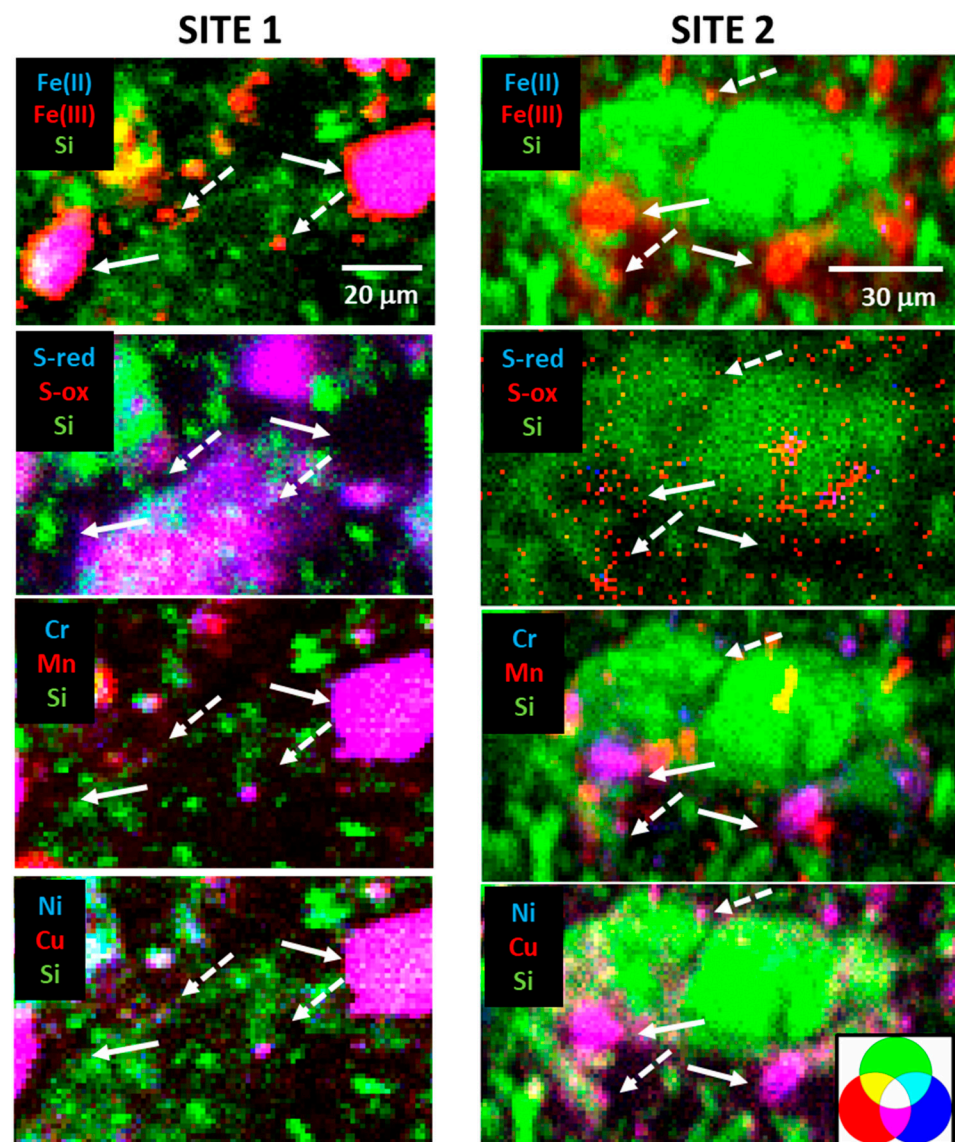


Figure 10. Representative μ -XRF images for discrete Fe oxide particles ranging from larger grains (solid white arrows) to smaller grains (white-dashed arrows), including redox maps (for Fe and S) and element maps (for Si, Cr, Mn, Ni, and Cu) for the samples from site 1 (**left column**) and site 2 (**right column**). The Fe and S maps are shown as two-component images (Fe(II) and Fe(III); S_{red} and S_{ox}) plus Si for orientation relative to the other maps. The color key is shown at the bottom right.

4. Discussion

4.1. Factors That Control Pyrite Weathering, Potential Fe Transport, and Re-Precipitation

The formation of secondary Fe oxides observed in the mine soils is controlled by factors from a combination of processes: (1) the oxidative dissolution of primary pyrite or other metal sulfide grains; (2) whether or not Fe is transported away from the pyrite surface before secondary precipitation; and (3) local hydrogeochemical conditions that may favor a specific secondary Fe oxide and grain texture. With respect to pyrite weathering, although other metal sulfides have been observed in the coal shale deposits within this watershed, pyrite is the dominant metal-bearing sulfide [36]. Broadly, sulfide mineral composition, morphology, particle size, reactive surface area, and texture control the oxidative dissolution-driven transformations and are typically dominated by the weathering of large (mm scale) crystals on surfaces within cracks in the grains [37]. It has been shown that for the oxidative dissolution of pyrite, a surface charge transfer to absorbed O_2 has been demonstrated to be

the rate-limiting step in the overall reaction [38]. Further, the oxygen in the sulfate reaction product has been shown to originate from water as a direct consequence of electrochemical mechanisms [39]. The combined effect of these processes provides support for the lack of complete pyrite weathering in shallow soils that are O₂-rich environments when the diffusion of H₂O may be limited, including relatively thin (<5 µm) surface coatings over pyrite (Figure 2A,B). Further, larger pyrite grains can remain unoxidized due the presence of thicker (10–20 µm) coatings that would limit both O₂ and H₂O diffusion (Figure 2C). The slower weathering of these grains within the coal shale matrix can persist decades after the bulk of the pyrite has been lost [40,41]. The pseudomorphic replacement of pyrite with Fe oxides has been shown to be the result of the limited diffusion of O₂ and subsequent transport of byproducts [42] and/or under a more buffered system (circumneutral to slightly alkaline) [43], even where aqueous Fe(III) concentrations are very low [44].

When pyrite oxidative dissolution coupled with Fe transport away from the pyrite surface does occur, the formation of secondary Fe oxides is controlled by local hydrogeochemical conditions, including pH and other pore water composition variables and flow parameters that range from the pore scale to the pedon scale [19]. With respect to pore water composition, higher sulfate concentrations (up to 3 g L⁻¹) and lower pH (2.5 to 4) values can result in the precipitation of schwertmannite and jarosite [45–47], and the formation of these phases can be strongly microbially mediated [48]. Following the precipitation of these metastable Fe(III)-bearing sulfates, jarosite and schwertmannite may either dissolve or transform into more ordered phases at higher pH values, particularly as pore water sulfate decreases over time as pyrite oxidation progresses. Sulfate-poor phases, such as ferrihydrite forming between pH 2 and pH 5, can form from direct Fe(III) precipitation and/or reprocessing of Fe(III) sulfates and typically go through further transformations into goethite at higher pH values (~5) and hematite at higher pH values (~7) [17]. The presence of both sulfate-rich and sulfate-poor Fe oxides in the current work (Figures 7 and 9) highlight the heterogeneous nature of the mine soils and complex precipitation pathways that could potentially be simultaneously present at the sub-mm scale.

With respect to the formation of secondary Fe oxide coatings versus discrete particles, it is possible that the discrete particles formed from the re-precipitation of the Fe downgradient from where it was originally released whereas coatings formed on or in closer proximity to the original pyrite grain [49]. This process may be coupled with transport through tight pore spaces that may favor Fe precipitation and aggregation in clay-rich regions [50,51]. More rapid precipitation due to the mixing of pore water with different compositions [52], rather than slower changes in an isolated pore water system, may also favor the precipitation of smaller grains either as discrete grains and/or within coatings. Further, the acid generated via the oxidation of pyrite can drive changes in its physical properties (e.g., porosity, permeability, and grain size distribution), which can affect solute transport [53], resulting in a continually changing landscape for Fe transport and re-precipitation. In the current work, both thicker secondary coatings (Figure 7) and larger particles (Figure 9) were sulfate rich, whereas smaller grains and thinner coatings were sulfate poor. It is possible that the sulfate-rich Fe oxides reflect an early post-pyrite weathering stage (when pore water sulfate concentrations are higher), and the sulfate-poor Fe oxides reflect later reworking of the Fe oxides.

4.2. Fate of Trace Metals

The re-sequestration of trace metals following their release from pyrite weathering results in the enrichment of these metals in secondary Fe oxides [54–56]. The relative enrichment of trace metals here (Mn > Cr > Ni > Cu) was also consistent with trace element concentrations in mine soils at the same site [25], indicating that grain- and sub-grain-scale reactions can control trace metal distribution at the pedon scale and is consistent with previous work [57–59]. In the current work, the discrete particles were observed to enrich these metals to a greater degree than the other secondary phases (Figure 4). Conversely, previous work has shown that trace metals are preferentially associated with

smaller grains with higher surface areas [60,61]. Further, metal uptake was also dependent on Fe oxide composition and size, with Cu associated with sulfate-poor grains, Ni with sulfate-rich grains, and Mn and Cr associated with larger grains (Figure 10). With respect to composition, a range of observations have been reported; for example, Fe(III) sulfates such as schwertmannite have been shown to have a limited divalent metal uptake ability during precipitation, but their subsequent transformation into goethite can result in metal uptake and retention [62]. In contrast, Cu has been shown to be preferentially sequestered by goethite and jarosite, while Ni and Zn accumulate in poorly crystalline schwertmannite [63]. With respect to particle size, we could not resolve as to whether Mn is present as separate Mn-bearing phases (e.g., Mn oxides) or present as Mn-bearing Fe oxides, although both have been previously identified in similar mine spoils [64]. It has also been shown that Cr uptake by Mn-bearing Fe oxides can exceed that of non-doped Fe oxides [65], which may explain the preferential accumulation of Cr by the larger, discrete Mn-bearing Fe oxides observed here (Figure 10). The summation of these results and comparison to previous work highlight the heterogeneous nature of mine soils and the complex relationship between hydrogeochemical factors that can drive mineral precipitation and metal uptake.

Comparisons of the concentrations of trace metals in the parent coal shale and the mine soils can also provide insights into the long-term dynamics that control metal transport versus retention. The concentrations of Cr, Mn, Ni, and Cu in the parent coal shale material are 2183 ppm, 768 ppm, 1500 ppm, and 90 ppm, respectively [35], and the concentrations in the bulk mine soils, and reflected in the grain- and sub-grain-scale analyses presented here, are 400 ppm, 2 wt.%, 75 ppm, and 50 ppm, respectively [25]. These results indicate that in the decades since waste emplacement, Mn has become enriched in the mine soils, whereas Cr, Ni, and Cu are slowly being leached. Similar results were observed in mine wastes, in which trace metals slowly continued to leach out after three decades since emplacement [66]. This is in contrast with previous work that has shown that Ni and Zn can accumulate in coal mine soils while Cu is leached [67]. These results highlight the need to integrate mine soil mineralogy and hydrogeochemistry to properly assess the long-term risk of metal leaching.

5. Conclusions

Analyses of near-surface mine spoils indicated the presence of pyrite as well as secondary Fe oxides that range in their grain size, texture, and morphology. The presence of a range of metal-bearing Fe(II) and Fe(III) phases highlights the chemically and physically complex heterogeneity in coal mine soils. Further, the presence of pyrite also indicates that the oxidative exhaustion of pyrite has yet to occur, despite nearly seven decades since the emplacement of the waste material, which is likely a direct result of the grain-scale complexity observed in the soils. Our results also underscore the potential importance of vegetation in driving weathering; for example, a previous study on forested sulfide mine waste showed little sulfide remaining after 40 years since emplacement [68], whereas a relatively unvegetated mine spoil site retained primary sulfides after more than 100 years since emplacement [69]. Increased organic matter content and plant activity can also lead to the long-term stabilization of metals within mine soils [70]. We have shown here that re-sequestration was dependent on grain size and morphology, and that the large, discrete Fe oxides were the most enriched in trace metals that originated from the pyrite. However, trace metals in the smaller particles and finer-grained secondary mineral coatings likely represent a more labile pool of trace metals that could be re-mobilized if local (bio)geochemical conditions were to shift. For example, during prolonged periods of saturation and reducing conditions, the fine-grained materials would be more likely to experience reductive dissolution [71,72]. Trends in metal enrichment (Mn) and depletion (Cr, Ni, and Cu) highlight the need for understanding metal speciation and distribution across scales in order to predict future metal transport.

Author Contributions: Conceptualization, M.A.R.C. and D.M.S.; methodology, M.A.R.C. and D.M.S.; validation, M.A.R.C. and D.M.S.; formal analysis, M.A.R.C. and D.M.S.; investigation, M.A.R.C. and

D.M.S.; resources, D.M.S.; data curation, D.M.S.; writing—original draft preparation, M.A.R.C. and D.M.S.; writing—review and editing, M.A.R.C. and D.M.S.; visualization, M.A.R.C. and D.M.S.; supervision, D.M.S.; project administration, D.M.S.; funding acquisition, D.M.S. All authors have read and agreed to the published version of the manuscript.

Funding: This research received no external funding.

Institutional Review Board Statement: Not applicable.

Informed Consent Statement: Not applicable.

Data Availability Statement: The data presented in this study are available on request from the corresponding author. The data are not publicly available due to the file size of the XMP data.

Acknowledgments: We would like to thank Matthew Newville, Tony Lanzirrotti, and the APS GeoSoilEnviroCARS (GSE-CARS) staff for their beamline support. GSE-CARS is supported by the National Science Foundation-Earth Sciences (EAR-1634415) and the Department of Energy-GeoSciences (DE-FG02-94ER14466). This study used resources from the Advanced Photon Source; a U.S. Department of Energy (DOE) Office of Science User Facility operated for the DOE Office of Science by Argonne National Laboratory under the contract no. DE-AC02-06CH11357. We thank the following KSU graduate students for their support in soil sample collection and μ -XRF analyses: Max Barczok, Daniel Wood, Kortney Cole, and Lindsey Yazbek. We also thank Marissa Lautzenheiser (Huff Run Watershed Restoration Partnership) for her logistical support at the study site.

Conflicts of Interest: The authors declare no conflict of interest.

References

1. Rouhani, A.; Skousen, J.; Tack, F.M.G. An Overview of Soil Pollution and Remediation Strategies in Coal Mining Regions. *Minerals* **2023**, *13*, 1064. [[CrossRef](#)]
2. Skousen, J.; Daniels, W.L.; Zipper, C.E. Soils on Appalachian coal-mined lands. In *Appalachia's Coal-Mined Landscapes: Resources and Communities in a New Energy Era*; Springer: Cham, Germany, 2021; pp. 85–109.
3. Clark, E.V.; Daniels, W.L.; Zipper, C.E.; Eriksson, K. Mineralogical influences on water quality from weathering of surface coal mine spoils. *Appl. Geochem.* **2018**, *91*, 97–106. [[CrossRef](#)]
4. Feng, Y.; Wang, J.; Bai, Z.; Reading, L. Effects of surface coal mining and land reclamation on soil properties: A review. *Earth-Sci. Rev.* **2019**, *191*, 12–25. [[CrossRef](#)]
5. Singer, D.M.; Herndon, E.; Cole, K.; Koval, J.; Perdrial, N. Formation of secondary mineral coatings and the persistence of reduced metal-bearing phases in soils developing on historic coal mine spoil. *Appl. Geochem.* **2020**, *121*, 104711. [[CrossRef](#)]
6. Maiti, S.K. *Ecorestoration of the Coalmine Degraded Lands*; Springer Science & Business Media: New York, NY, USA, 2013.
7. Kirby, B.; Vengadajellum, C.; Burton, S.; Cowan, D. Coal, coal mines and spoil heaps. In *Handbook of Hydrocarbon and Lipid Microbiology*; Springer: Berlin/Heidelberg, Germany, 2010.
8. Shrestha, R.K.; Lal, R. Ecosystem carbon budgeting and soil carbon sequestration in reclaimed mine soil. *Environ. Int.* **2006**, *32*, 781–796. [[CrossRef](#)]
9. Large, R.R.; Halpin, J.A.; Danyushevsky, L.V.; Maslennikov, V.V.; Bull, S.W.; Long, J.A.; Gregory, D.D.; Lounejeva, E.; Lyons, T.W.; Sack, P.J.; et al. Trace element content of sedimentary pyrite as a new proxy for deep-time ocean–atmosphere evolution. *Earth Planet. Sci. Lett.* **2014**, *389*, 209–220. [[CrossRef](#)]
10. Dang, Z.; Liu, C.; Haigh, M.J. Mobility of heavy metals associated with the natural weathering of coal mine spoils. *Environ. Pollut.* **2002**, *118*, 419–426. [[CrossRef](#)]
11. Mishra, S.; Bharagava, R.N.; More, N.; Yadav, A.; Zainith, S.; Mani, S.; Chowdhary, P. Heavy Metal Contamination: An Alarming Threat to Environment and Human Health. In *Environmental Biotechnology: For Sustainable Future*; Springer: Singapore, 2019; pp. 103–125. [[CrossRef](#)]
12. Neculita, C.M.; Rosa, E. A review of the implications and challenges of manganese removal from mine drainage. *Chemosphere* **2019**, *214*, 491–510. [[CrossRef](#)]
13. Lindsay, M.B.; Condon, P.D.; Jambor, J.L.; Lear, K.G.; Blowes, D.W.; Ptacek, C.J. Mineralogical, geochemical, and microbial investigation of a sulfide-rich tailings deposit characterized by neutral drainage. *Appl. Geochem.* **2009**, *24*, 2212–2221. [[CrossRef](#)]
14. Cravotta, C.A., III. Abandoned Mine Drainage in the Swatara Creek Basin, Southern Anthracite Coalfield, Pennsylvania, USA: 2. Performance of Treatment Systems. *Mine Water Environ.* **2010**, *29*, 200–216. [[CrossRef](#)]
15. Ross, M.R.V.; Nippgen, F.; Hassett, B.A.; McGlynn, B.L.; Bernhardt, E.S. Pyrite Oxidation Drives Exceptionally High Weathering Rates and Geologic CO₂ Release in Mountaintop-Mined Landscapes. *Glob. Biogeochem. Cycles* **2018**, *32*, 1182–1194. [[CrossRef](#)]
16. Cravotta, C.A. Dissolved metals and associated constituents in abandoned coal-mine discharges, Pennsylvania, USA. Part 1: Constituent quantities and correlations. *Appl. Geochem.* **2008**, *23*, 166–202. [[CrossRef](#)]
17. Cudennec, Y.; Lecerf, A. The transformation of ferrihydrite into goethite or hematite, revisited. *J. Solid State Chem.* **2006**, *179*, 716–722. [[CrossRef](#)]

18. Nicholson, R.V.; Gillham, R.; Reardon, E. Pyrite oxidation in carbonate-buffered solution: 2. Rate control by oxide coatings. *Geochim. et Cosmochim. Acta* **1990**, *54*, 395–402. [[CrossRef](#)]
19. Gu, X.; Heaney, P.J.; Reis, F.D.A.A.; Brantley, S.L. Deep abiotic weathering of pyrite. *Science* **2020**, *370*, eabb8092. [[CrossRef](#)]
20. Von der Heyden, B.P.; Roychoudhury, A.N. Application, chemical interaction and fate of iron minerals in polluted sediment and soils. *Curr. Pollut. Rep.* **2015**, *1*, 265–279. [[CrossRef](#)]
21. Ruiz-Agudo, C.; Putnis, C.V.; Ruiz-Agudo, E.; Putnis, A. The influence of pH on barite nucleation and growth. *Chem. Geol.* **2015**, *391*, 7–18. [[CrossRef](#)]
22. Buerge-Weirich, D.; Hari, R.; Xue, H.; Behra, P.; Sigg, L. Adsorption of Cu, Cd, and Ni on Goethite in the Presence of Natural Groundwater Ligands. *Environ. Sci. Technol.* **2002**, *36*, 328–336. [[CrossRef](#)]
23. Karapinar, N. Removal of Heavy Metal Ions by Ferrihydrite: An Opportunity to the Treatment of Acid Mine Drainage. *Water Air Soil Pollut.* **2016**, *227*, 1–8. [[CrossRef](#)]
24. Marescotti, P.; Carbone, C.; Comodi, P.; Frondini, F.; Lucchetti, G. Mineralogical and chemical evolution of ochreous precipitates from the Libiola Fe–Cu-sulfide mine (Eastern Liguria, Italy). *Appl. Geochem.* **2012**, *27*, 577–589. [[CrossRef](#)]
25. Wise, M. *Huff Run Watershed Plan*; Huff Run Watershed Restoration Partnership, Inc.: Mineral City, OH, USA, 2005.
26. Wood, D.L.; Cole, K.A.; Herndon, E.M.; Singer, D.M. Lime slurry treatment of soils developing on abandoned coal mine spoil: Linking contaminant transport from the micrometer to pedon-scale. *Appl. Geochem.* **2023**, *151*, 105617. [[CrossRef](#)]
27. Smart, K.E.; Singer, D.M. Surface Coal Mine Soils: Evidence for Chronosequence Development. *Soil Syst.* **2023**, *7*, 59. [[CrossRef](#)]
28. Singer, D.; Herndon, E.; Zemanek, L.; Cole, K.; Sanda, T.; Senko, J.; Perdrial, N. Biogeochemical Controls on the Potential for Long-Term Contaminant Leaching from Soils Developing on Historic Coal Mine Spoil. *Soil Syst.* **2021**, *5*, 3. [[CrossRef](#)]
29. Chowdhury, A.R.; Singer, D.M.; Herndon, E. Colloidal metal transport in soils developing on historic coal mine spoil. *Appl. Geochem.* **2021**, *128*, 104933. [[CrossRef](#)]
30. Chowdhury, M.A.R.; Singer, D.M. Trace Metal Enrichment in the Colloidal Fraction in Soils Developing on Abandoned Mine Spoils. *Minerals* **2022**, *12*, 1290. [[CrossRef](#)]
31. ODNR. Economic Impact Analysis of the Ohio Abandoned Mine Land Program. In *Ohio Department of Natural Resources Division of Mineral Resources Management*; Ohio University's Voinovich School of Leadership and Public Affairs: Athens, OH, USA, 2014.
32. ODNR. Huff Run Watershed Acid Mine Drainage Abatement and Treatment Plan; Prepared for Ohio DNR by Gannett Fleming. Available online: watersheddata.com (accessed on 7 December 2014).
33. Newville, M.; Sutton, S.R.; Rivers, M.L.; Eng, P. Micro-beam X-ray absorption and fluorescence spectroscopies at GSECARS: APS beamline 13ID. *J. Synchrotron Radiat.* **1999**, *6*, 353–355. [[CrossRef](#)]
34. Newville, M. Larch: An Analysis Package for XAFS and Related Spectroscopies. *J. Phys. Conf. Ser.* **2013**, *430*, 012007. [[CrossRef](#)]
35. Yazbek, L.D.; Cole, K.A.; Shedleski, A.; Singer, D.; Herndon, E.M. Hydrogeochemical Processes Limiting Aqueous and Colloidal Fe Export in a Headwater Stream Impaired by Acid Mine Drainage. *ACS ES&T Water* **2020**, *1*, 68–78. [[CrossRef](#)]
36. Singer, D.M.; Herndon, E.; Cole, K.; Burkey, M.; Morisson, S.; Cahill, M.; Bartucci, M.A. Micron-scale distribution controls metal(loid) release during simulated weathering of a Pennsylvanian coal shale. *Geochim. Cosmochim. Acta* **2020**, *269*, 117–135. [[CrossRef](#)]
37. Deditius, A.P.; Utsunomiya, S.; Reich, M.; Kesler, S.E.; Ewing, R.C.; Hough, R.; Walshe, J. Trace metal nanoparticles in pyrite. *Ore Geol. Rev.* **2011**, *42*, 32–46. [[CrossRef](#)]
38. Chiriță, P.; Schlegel, M.L. Pyrite oxidation in air-equilibrated solutions: An electrochemical study. *Chem. Geol.* **2017**, *470*, 67–74. [[CrossRef](#)]
39. Holmes, P.R.; Crundwell, F.K. The kinetics of the oxidation of pyrite by ferric ions and dissolved oxygen: An electrochemical study. *Geochim. et Cosmochim. Acta* **2000**, *64*, 263–274. [[CrossRef](#)]
40. Ruppert, L.F.; Hower, J.C.; Eble, C.F. Arsenic-bearing pyrite and marcasite in the Fire Clay coal bed, Middle Pennsylvanian Breathitt Formation, eastern Kentucky. *Int. J. Coal Geol.* **2005**, *63*, 27–35. [[CrossRef](#)]
41. Diehl, S.; Goldhaber, M.; Koenig, A.; Lowers, H.; Ruppert, L. Distribution of arsenic, selenium, and other trace elements in high pyrite Appalachian coals: Evidence for multiple episodes of pyrite formation. *Int. J. Coal Geol.* **2012**, *94*, 238–249. [[CrossRef](#)]
42. Gu, X.; Rempe, D.M.; Dietrich, W.E.; West, A.J.; Lin, T.-C.; Jin, L.; Brantley, S.L. Chemical reactions, porosity, and microfracturing in shale during weathering: The effect of erosion rate. *Geochim. Cosmochim. Acta* **2020**, *269*, 63–100. [[CrossRef](#)]
43. Huminicki, D.M.; Rimstidt, J.D. Iron oxyhydroxide coating of pyrite for acid mine drainage control. *Appl. Geochem.* **2009**, *24*, 1626–1634. [[CrossRef](#)]
44. Rusch, B.; Hanna, K.; Humbert, B. Coating of quartz silica with iron oxides: Characterization and surface reactivity of iron coating phases. *Colloids Surf. A Physicochem. Eng. Asp.* **2010**, *353*, 172–180. [[CrossRef](#)]
45. Kim, H.-J.; Kim, Y. Schwertmannite transformation to goethite and the related mobility of trace metals in acid mine drainage. *Chemosphere* **2021**, *269*, 128720. [[CrossRef](#)]
46. Fitzpatrick, R.; Mosley, L.; Raven, Shand, P. Schwertmannite formation and properties in acidic drain environments following exposure and oxidation of acid sulfate soils in irrigation areas during extreme drought. *Geoderma* **2017**, *308*, 235–251. [[CrossRef](#)]
47. Chen, Q.; Cohen, D.R.; Andersen, M.S.; Robertson, A.M.; Jones, D.R. Stability and trace element composition of natural schwertmannite precipitated from acid mine drainage. *Appl. Geochem.* **2022**, *143*, 105370. [[CrossRef](#)]
48. Bigham, J.; Schwertmann, U.; Traina, S.; Winland, R.; Wolf, M. Schwertmannite and the chemical modeling of iron in acid sulfate waters. *Geochim. Cosmochim. Acta* **1996**, *60*, 2111–2121. [[CrossRef](#)]

49. Uzarowicz, Ł.; Skiba, S. Technogenic soils developed on mine spoils containing iron sulphides: Mineral transformations as an indicator of pedogenesis. *Geoderma* **2011**, *163*, 95–108. [[CrossRef](#)]
50. Duiker, S.W.; Rhoton, F.E.; Torrent, J.; Smeck, N.E.; Lal, R. Iron (hydr) oxide crystallinity effects on soil aggregation. *Soil Sci. Soc. Am. J.* **2003**, *67*, 606–611. [[CrossRef](#)]
51. Zhang, W.; Tang, X.-Y.; Xian, Q.-S.; Weisbrod, N.; Yang, J.E.; Wang, H.-L. A field study of colloid transport in surface and subsurface flows. *J. Hydrol.* **2016**, *542*, 101–114. [[CrossRef](#)]
52. Akcil, A.; Koldas, S. Acid Mine Drainage (AMD): Causes, treatment and case studies. *J. Clean. Prod.* **2006**, *14*, 1139–1145. [[CrossRef](#)]
53. Navarre-Sitchler, A.; Steefel, C.I.; Yang, L.; Tomutsa, L.; Brantley, S.L. Evolution of porosity and diffusivity associated with chemical weathering of a basalt clast. *J. Geophys. Res.* **2009**, *114*, 100. [[CrossRef](#)]
54. Bigham, J.M.; Nordstrom, D.K. Iron and Aluminum Hydroxysulfates from Acid Sulfate Waters. *Rev. Miner. Geochem.* **2000**, *40*, 351–403. [[CrossRef](#)]
55. Filipek, L.H.; Nordstrom, D.K.; Ficklin, W.H. Interaction of acid mine drainage with waters and sediments of West Squaw Creek in the West Shasta Mining District, California. *Environ. Sci. Technol.* **1987**, *21*, 388–396. [[CrossRef](#)]
56. Jambor, J.L.; Nordstrom, D.K.; Alpers, C.N. Metal-sulfate salts from sulfide mineral oxidation. *Rev. Mineral. Geochem.* **2000**, *40*, 303–350. [[CrossRef](#)]
57. Li, H.; Ji, H.; Shi, C.; Gao, Y.; Zhang, Y.; Xu, X.; Ding, H.; Tang, L.; Xing, Y. Distribution of heavy metals and metalloids in bulk and particle size fractions of soils from coal-mine brownfield and implications on human health. *Chemosphere* **2017**, *172*, 505–515. [[CrossRef](#)]
58. Strawn, D.G.; Hickey, P.J.; McDaniel, P.A.; Baker, L.L. Distribution of As, Cd, Pb, and Zn in redox features of mine-waste impacted wetland soils. *J. Soils Sediments* **2012**, *12*, 1100–1110. [[CrossRef](#)]
59. Lanzirrotti, A.; Tappero, R.; Schulze, D.G. Chapter 2-Practical Application of Synchrotron-Based Hard X-Ray Microprobes in Soil Sciences. In *Developments in Soil Science*; Singh, B., Gräfe, M., Eds.; Elsevier: Amsterdam, The Netherlands, 2010; pp. 27–72.
60. Horowitz, A.J.; Elrick, K.A. The relation of stream sediment surface area, grain size and composition to trace element chemistry. *Appl. Geochem.* **1987**, *2*, 437–451. [[CrossRef](#)]
61. Luoma, S.N. Processes affecting metal concentrations in estuarine and coastal marine sediments. In *Heavy Metals in the Marine Environment*; CRC Press: Boca Raton, FL, USA, 2018; pp. 51–66.
62. Acero, P.; Ayora, C.; Torrentó, C.; Nieto, J.-M. The behavior of trace elements during schwertmannite precipitation and subsequent transformation into goethite and jarosite. *Geochim. Cosmochim. Acta* **2006**, *70*, 4130–4139. [[CrossRef](#)]
63. Sidenko, N.V.; Sherriff, B.L. The attenuation of Ni, Zn and Cu, by secondary Fe phases of different crystallinity from surface and ground water of two sulfide mine tailings in Manitoba, Canada. *Appl. Geochem.* **2005**, *20*, 1180–1194. [[CrossRef](#)]
64. Herndon, E.; Yarger, B.; Frederick, H.; Singer, D. Iron and Manganese Biogeochemistry in Forested Coal Mine Spoil. *Soil Syst.* **2019**, *3*, 13. [[CrossRef](#)]
65. Ghosh, A.; Pal, M.; Biswas, K.; Ghosh, U.C.; Manna, B. Manganese oxide incorporated ferric oxide nanocomposites (MIFN): A novel adsorbent for effective removal of Cr(VI) from contaminated water. *J. Water Process. Eng.* **2015**, *7*, 176–186. [[CrossRef](#)]
66. Clark, E.V.; Zipper, C.E.; Daniels, W.L.; Keefe, M.J. Appalachian coal mine spoil elemental release patterns and depletion. *Appl. Geochem.* **2018**, *98*, 109–120. [[CrossRef](#)]
67. Gao, X.; Xu, M.; Hu, Q.; Wang, Y. Leaching behavior of trace elements in coal spoils from Yangquan coal mine, Northern China. *J. Earth Sci.* **2016**, *27*, 891–900. [[CrossRef](#)]
68. Beauchemin, S.; Langley, S.; MacKinnon, T. Geochemical properties of 40-year old forested pyrrhotite tailings and impact of organic acids on metal cycling. *Appl. Geochem.* **2019**, *110*, 104437. [[CrossRef](#)]
69. Adams, R.; Ahlfeld, D.; Sengupta, A. Investigating the Potential for Ongoing Pollution from an Abandoned Pyrite Mine. *Mine Water Environ.* **2007**, *26*, 2–13. [[CrossRef](#)]
70. Hammond, C.M.; Root, R.A.; Maier, R.M.; Chorover, J. Metal Lability and Mass Transfer Response to Direct-Planting Phytostabilization of Pyritic Mine Tailings. *Minerals* **2022**, *12*, 757. [[CrossRef](#)]
71. Larsen, O.; Postma, D. Kinetics of reductive bulk dissolution of lepidocrocite, ferrihydrite, and goethite. *Geochim. et Cosmochim. Acta* **2001**, *65*, 1367–1379. [[CrossRef](#)]
72. Anschutz, A.J.; Penn, R.L. Reduction of crystalline iron(III) oxyhydroxides using hydroquinone: Influence of phase and particle size. *Geochem. Trans.* **2005**, *6*, 60. [[CrossRef](#)]

Disclaimer/Publisher’s Note: The statements, opinions and data contained in all publications are solely those of the individual author(s) and contributor(s) and not of MDPI and/or the editor(s). MDPI and/or the editor(s) disclaim responsibility for any injury to people or property resulting from any ideas, methods, instructions or products referred to in the content.